Journal of Catalysis 282 (2011) 35–46

Contents lists available at ScienceDirect

Journal of Catalysis

journal homepage: www.elsevier.com/locate/jcat

Effect of pretreatment on precipitated Fe–Mo Fischer–Tropsch catalysts: Morphology, carburization, and catalytic performance

Xiaojing Cui [a,b,c], Jian Xu [b,*], Chenghua Zhang [a,b], Yong Yang [a,b], Peng Gao [b], Baoshan Wu [a,b], Yongwang Li [a,b,*]

[a] State Key Laboratory of Coal Conversion, Institute of Coal Chemistry, Chinese Academy of Sciences, Taiyuan 030001, People's Republic of China
[b] National Engineering Laboratory for Indirect Coal Liquefaction, Institute of Coal Chemistry, Chinese Academy of Sciences, Taiyuan 030001, People's Republic of China
[c] Graduate School of the Chinese Academy of Sciences, Beijing 100039, People's Republic of China

ARTICLE INFO

Article history:
Received 24 January 2011
Revised 10 May 2011
Accepted 18 May 2011
Available online 26 July 2011

Keywords:
Fischer–Tropsch synthesis
Iron
Molybdenum
Pretreatment
Mo migration effect

ABSTRACT

Unpromoted and Mo-promoted iron catalyst precursors (100Fe, 100Fe5Mo, and 100Fe10Mo) were prepared by a coprecipitation method, and were subsequently characterized by laser Raman spectroscopy, Mössbauer spectroscopy, at 298 K and 20 K, X-ray photoelectron spectroscopy, and high-resolution transmission electron microscopy. The effect of pretreatment with H_2, CO, and H_2/CO = 0.67 at 280 and 350 °C was investigated. Specifically, the reduction/carburization behaviors and the evolution of iron phases and Mo species in the catalysts during the pretreatment and during the FTS reaction were extensively studied. During pretreatment, the catalyst structure experienced an extensive restructuring process that was strongly dependent on the pretreatment protocols and Mo promoter loading levels. The microscopic information confirmed this effect on the iron active-site dispersion and the catalytic performance.

1. Introduction

Fischer–Tropsch synthesis (FTS) as an important route to convert the carbon-derived syngas to liquid fuels is considered as a promising and practical industrial solution to the short-term fuel shortage [1]. Iron-based FTS catalysts are used industrially due to their low cost, low methane selectivity, and high activity [1,2]. Two of the principal challenges in FTS catalyst technology are catalyst stabilization under the rigorous reaction conditions and control of product selectivity to products of interest. Up to now, the most effective approaches reported in the literature include the modification of iron catalyst precursors with other metal promoters [3–5] or supports [6], the design of pretreatment protocols [7–19], and a combination of these methods.

A large number of studies concerning pretreatment effects on Fe FTS catalysts have been carried out to unravel the relationships between catalyst textural properties, phase transformations, and FTS performance. For example, in a pretreatment study with a precipitated Fe/Cu/K/Si catalyst (100Fe3Cu4K16SiO_2 by mass) using a stirred tank slurry reactor (STSR) by Bukur et al. [10], the correlations of the bulk iron phases, the average sizes of iron crystallites and the amount of carbon deposits formed during the pretreatment procedures with catalyst activity were established. They concluded that the H_2 pretreated catalysts produced more methane and gaseous hydrocarbons (C_2–C_4) than the CO and syngas pretreated catalysts. Shroff et al. [11] investigated the transformation of bulk structure and microstructure of a commercial Fe/Cu/K catalyst activated in various pretreatment gases (H_2, CO, and H_2/CO = 0.7). They observed a decrease in the size of iron crystallites as the catalyst was activated in CO or H_2/CO = 0.7; i.e., the magnetite was broken down into smaller iron carbide nodules separated by the carbon deposits [11].

Recently, facilitated by modern catalyst characterization techniques such as Mössbauer spectroscopy (MES) [20], X-ray photoelectron spectroscopy (XPS) [20], temperature-programmed hydrogenation (TPH) [21], in situ diffuse reflectance Fourier transform infrared spectroscopy (DR-FTIR) [22,23], and high-resolution transmission electron microscopy (HRTEM) [11], numerous descriptive evolution models of bulk and surface compositions have been proposed for unsupported and supported iron FT catalysts pretreated in H_2 [11,21], syngas [21,24], or CO [21]. In summary, the iron oxide (Fe_2O_3) is first reduced to magnetite (Fe_3O_4), irrespective of activation gas type, accompanied by the nucleation of Fe_3O_4 grains oriented from the surfaces to the cores of Fe_2O_3 particles, leading to the agglomeration of the catalyst skeleton [11,21]. Further transformation of Fe_3O_4 to iron carbides in CO or syngas is achieved by the breakdown of the crystallites of Fe_3O_4 to smaller crystallites of iron carbide [11,21,24].

In addition, molybdenum metal [25] and carbide [26–28] were reported to show excellent hydrogenation/isomerization activity

* Corresponding authors. Addresses: National Engineering Laboratory for Indirect Coal Liquefaction, Institute of Coal Chemistry, Chinese Academy of Sciences, Taiyuan 030001, People's Republic of China. Fax: +86 351 7560668 (J. Xu), State Key Laboratory of Coal Conversion, Institute of Coal Chemistry, Chinese Academy of Sciences, Taiyuan 030001, People's Republic of China. Fax: +86 351 4124899 (Y.-W. Li).

E-mail addresses: xujian@synfuelschina.com.cn (J. Xu), ywl@sxicc.ac.cn (Y.-W. Li).

0021-9517/$ - see front matter © 2011 Elsevier Inc. All rights reserved.
doi:10.1016/j.jcat.2011.05.020

and moderate FTS activity. The introduction of Mo promoter should shift the FTS product spectrum to light hydrocarbons and reduce the catalyst deactivation caused by coke. Although the bimetallic FeMo FTS catalyst system is potentially an important choice for indirect coal liquefaction, considering its excellent stability and high selectivities to gasoline-range light hydrocarbons [29–31], pretreatment effect studies on the FeMo bimetallic system are scarce and scattered [32]. Depending on the Mo loading and catalyst preparation methods, the Mo promoter in an iron-based catalyst exhibits two effects, namely a bimetallic coverage effect and a physical dispersion effect [29,32]. Specifically, the bimetallic coverage effect decreases the available active iron surface area either by inert dilution or by covering active iron sites [32], while the physical segregation effect reduces the particle size of active iron sites (or active iron ensembles) and hence improves dispersion of active iron sites [29]. In previous studies [29–33], the introduction of the support and/or another metal promoter(s) into the FeMo catalyst matrix made it more difficult to clearly understand the interactions between Fe and Mo. Hence, it is a logical sequence to start from the basic FeMo bimetallic precursors before further studies are carried out on the supported FeMo or the multiple-metal catalyst system.

To differentiate the structural evolution of the highly dispersed Fe phases from that of the Mo promoter, numerous classic works have demonstrated the advantages of Mössbauer spectroscopy at cryogenic temperatures in studying highly dispersed iron or iron bimetallic systems, the spectra of which could be considerably improved for studying iron magnetism and lattice dynamics [34,35]. Owing to the particle size distribution of the nanometer-range particles, superparamagnetism and decreased magnetic splitting can be observed at room temperature and 77 K, respectively. Taking advantage of the strong temperature dependence of the superparamagnetism relaxation time, earlier work by Amelse [36] and Niemantsverdriet [34] has demonstrated the applicability of liquid helium Mössbauer spectroscopy in the study of a series of important bimetallic Fe systems, such as FeNi [37], FeCu, FeCo [36], and FeRu/FeRh/FePd/FeIr/FePt systems [38].

Moreover, Kündig and Bömmel [39], Mørup [40–43], and Bødker [44,45] developed low-temperature Mössbauer spectroscopy into an elegant quantitative method in measuring the particle sizes of hematite, magnetite nanoparticles, and amorphous iron carbides ($Fe_{1-x}C_x$), where superparamagnetic relaxation was analyzed using the Néel–Brown expression,

$$\tau = \tau_0 \exp(KV/kT),$$

where K is the magnetic anisotropy energy constant, V is the particle volume, k is Boltzmann's constant and T is the temperature. This equation can be used to yield a particle size distribution of a nanosized sample if K is known and assumed to be independent of the temperature. Furthermore, when spectra for a nanosized sample are measured at progressively lower temperatures, the average blocking temperature (T_B) at which half of the particles exhibit superparamagnetic (SPM) relaxation can be obtained, from which the average size can be conveniently estimated with the following formula [46]:

$$KV/kT_B = 4.5.$$

Consequently, the present work aimed at the elucidation of the effect of pretreatment protocols, including pretreatment temperature and pretreatment gas type, on the structure, carburization, and FTS performance of bimetallic FeMo catalysts. A series of FeMo bimetallic catalyst precursors were prepared for better understanding of the promotional effect of Mo on the Fe FTS catalyst. The selected FeMo bimetallic catalyst precursors were then pretreated in H_2, CO, or syngas (H_2/CO = 0.67) at various pretreatment temperatures (280 or 350 °C) followed by the FTS reaction under H_2/CO = 1.6, 280 °C, and 1.5 MPa. The structure evolution and reduction/carburization behavior of Fe and FeMo catalysts were characterized by XPS, MES, and HRTEM. Particular attention was paid to the identification of the Mo phases in the iron catalyst as well as evolutions of their promotional effects during the pretreatment.

2. Experimentals and methods

2.1. Catalyst preparation

Iron–molybdenum catalysts with a variety of Fe/Mo ratios were prepared by the coprecipitation method with iron nitrate, $Fe(NO_3)_3{\cdot}9H_2O$, and ammonium heptamolybdate, $(NH_4)_6Mo_7O_{24}{\cdot}4H_2O$. The ammonium heptamolybdate and iron nitrate solutions were preheated to 80 °C. The iron nitrate solution was added into a solution of ammonium heptamolybdate (pH = 2). The NH_4OH was then added dropwise into the mixed solution until a pH of 6 was reached. The temperature was kept at 80 °C during the whole precipitation process. The iron and molybdenum precipitate thus obtained was aged under vigorous stirring at 90 °C for 3 h, followed by filtering and drying at 120 °C for 48 h. The catalyst samples were then calcinated at 375 °C for 10 h. The unpromoted iron catalyst was obtained from the precipitated iron nitrate according to the method described above. The prepared catalysts were designated as 100Fe for the unpromoted iron catalyst, and 100Fe5Mo, 100Fe8Mo, and 100Fe10Mo for the iron–molybdenum bimetallic catalyst precursors with different levels of molybdenum promoters.

2.2. Catalyst characterization

Laser Raman spectroscopy (LRS) was obtained by a Renishaw–UV–vis Raman System 1000 using CCD as the detector and a green argon ion laser (λ = 514.4 nm) as the ray source, that was set to an output power of 7 mW.

X-ray photoelectron spectroscopy analysis was performed in a VG MultiLab 2000 instrument using Mg Kα primary radiation source. All binding energies were referenced to C1*s* of 284.6 eV. An estimated error of ±0.1 eV can be assumed for all the measurements. The ex situ XPS spectra of Mo 3*d* peaks in pretreated catalysts were fitted using a nonlinear least-squares method with a Lorentzian–Guassian function.

All Mössbauer spectra of fresh, pretreated, and spent catalysts were collected at 298 K and 20 K with a CANBERRA series 40 MCA constant-acceleration drive with a triangular reference signal. The γ-ray source was a ^{57}Co-in-Pd matrix. Data analysis was performed using a nonlinear least-squares fitting procedure with a set of independent Lorentzian lines including singlets, quadruple doublets and/or magnetic sextets.

HRTEM characterization was performed at a JEOL 2010 HRTEM (JEOL, Japan) using an accelerating voltage of 200 kV. The calcined and passivated catalyst samples were dispersed in ethanol and mounted on a carbon foil supported on a copper grid.

The standard passivation for all the pretreated and post mortem catalysts was strictly controlled, which involved (1) cooling down to room temperature in the pretreatment gas and in the reaction syngas (H_2/CO = 1.6) respectively; (2) flushing with a 1% O_2–99% He (mol/mol) gas stream until a small temperature rise was observed (typically 1–4 °C); and (3) finally, flushing with a stream of 5% O_2–95% He (mol/mol) before exposure to air.

2.3. Catalyst testing

A detailed description of the reactor and the product collection system used in this study was given elsewhere [47,48]. Typically, 2 g of the catalyst precursor was mixed with 20–40 mesh quartz

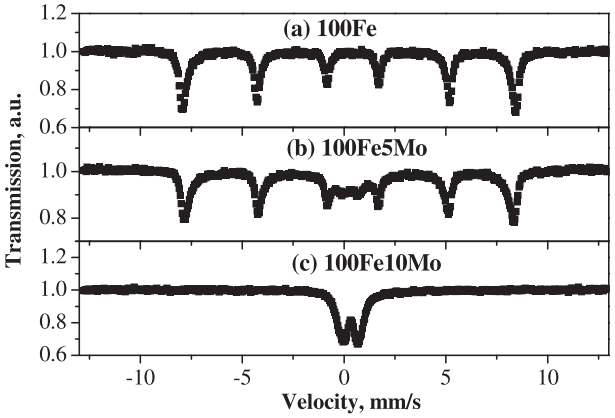

Fig. 1. Mössbauer spectra of the catalyst precursors: (a) 100Fe; (b) 100Fe5Mo; (c) 100Fe10Mo.

granules in all FTS tests. A portion of 3 cm^3 of the mixture was loaded into the isothermal section of the reactor. Prior to the reaction, all catalyst precursors were pretreated in situ with a stream of H_2, CO, or syngas (H_2/CO = 0.67) under 280 or 350 °C, 1 atm, and 6 NL/g-cat/h for 12 h. Following activation, the reactor was cooled to 200 °C. The system was then pressurized with the reaction syngas (H_2/CO = 1.6) up to 1.5 MPa. The temperature was gradually increased to 280 °C. Afterward, the FTS reaction was carried out in a flow of the reaction syngas at 280 °C and 3 NL/g-cat/h. Both the purified feed gases and the tail gas were analyzed by online gas chromatographs (GCs, Models 6890N and 4890D; Agilent), and the flow rate was measured by a wet-gas flowmeter.

3. Results and discussion

3.1. Structure of the catalyst precursors

3.1.1. Characterization by MES

The Mössbauer spectra of all catalyst precursors are displayed in Fig. 1. Only a sextet appeared in 100Fe catalyst, indicating that a nearly pure bulk phase of paramagnetic α-Fe_2O_3 with particle size larger than 13.5 nm exists in this catalyst [3], while for 100Fe5Mo catalyst, in addition to a sextet of the main α-Fe_2O_3 phase, two doublets showed up in the centroid of the spectrum, which were attributed to iron oxides with crystallite sizes smaller than 13.5 nm [3]. Surprisingly, only a doublet of superparamagnetic Fe^{3+} species appeared in 100Fe10Mo catalyst, suggesting the existence of highly dispersed iron oxide particles. It is also noteworthy that FeMo catalyst precursors exhibited smaller HFS values than 100Fe catalyst (results are not shown in this paper), which can be attributed to the magnetic dilution of Fe^{3+} by Mo^{6+} [49]. To evaluate the size distributions of hematite crystallites in the 100Fe10Mo, Mössbauer spectra were measured at progressively lower temperatures, from which the percentage of the superparamagnetic α-Fe_2O_3 as a function of temperature was obtained (see Fig. S1). The size distribution of the 100Fe10Mo was calculated using an effective anisotropy constant (K) value of $(4.7 \pm 1.2) \times 10^3$ J/m^3 [39]. As shown in Fig. S1, the average diameter of the hematite in the 100Fe10Mo was evaluated to be 11 nm.

3.1.2. Characterization by HRTEM

HRTEM images of the catalysts are displayed in Fig. 2. The iron oxides in 100Fe5Mo and 100Fe10Mo catalysts exhibited a lattice spacing ranging from 2.58 to 2.56 Å, corresponding to the

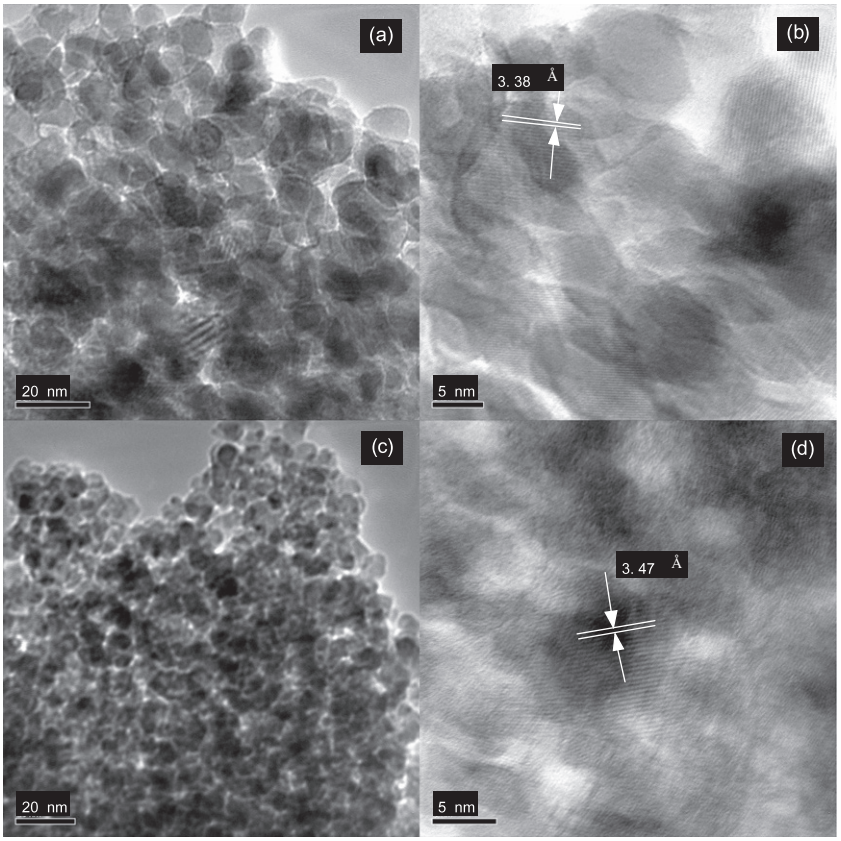

Fig. 2. HRTEM micrographs of iron–molybdenum catalyst precursors: (a, b) 100Fe5Mo; (c, d) 100Fe10Mo.

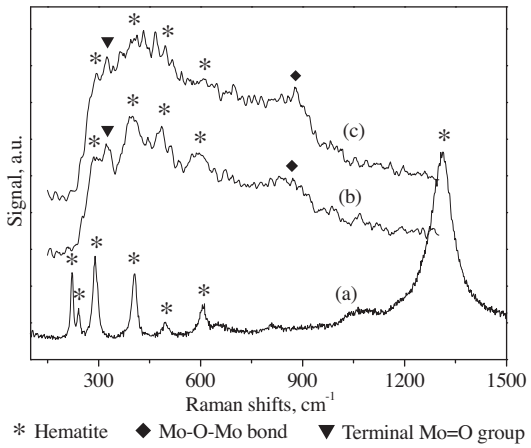

Fig. 3. Laser Raman spectra of the catalyst precursors: (a) 100Fe; (b) 100Fe5Mo; (c) 100Fe10Mo.

interplanar spacing of the (104) plane of α-Fe_2O_3. The average size of α-Fe_2O_3 in the 100Fe5Mo catalyst was ca. 12 nm, while a fairly uniform iron particle size of 6 nm was observed in the 100Fe10Mo catalyst (Fig. 2a and c). This decrease in the particle size in the 100Fe10Mo catalyst matches well with the MES observations. The Mo species in both FeMo catalysts were identified to be MoO_3 particles with a lattice spacing ranging from 3.38 Å to 3.47 Å corresponding to the *d*-values of the (0 0 2) plane of MoO_3 (Fig. 2b and d). These MoO_3 particles were randomly shaped islands with amorphous form or short-range order. The average size of MoO_3 in 100Fe5Mo was estimated to be 8 nm, while that in 100Fe10Mo was evaluated to be 7 nm.

3.1.3. Characterization by LRS

The Mo phases in the catalyst precursors were further identified by LRS characterization (see Fig. 3). The spectrum of 100Fe catalyst consisted of peaks located at 221.9, 240.4, 289.2, 405.3, 496.1, 610.5, and 1312.7 cm^{-1}, which were characteristic of the α-Fe_2O_3 phase [50]. However, the intensity of these peaks decreased drastically with increased Mo loading. Specifically, the peaks at ca. 221.9, 240.4, and 1312.7 cm^{-1} disappeared, while a new peak at 323–326 cm^{-1} appeared in the spectra of the FeMo catalysts, which was ascribed to the bending vibrations of terminal Mo=O bonds [51]. Meanwhile, a peak centered at ca. 863–878 cm^{-1} showed up in the spectra of the 100Fe5Mo and 100Fe10Mo catalysts, corresponding to the stretching of the Mo–O–Mo bond of the surface polymolybdate species [52]. The 866 cm^{-1} peak can be assigned to the highly dispersed surface polymolybdate species located beside or atop the iron oxide particles. The increasing intensity of this peak with increased in Mo loading indicated that the surface molybdate species were more prevalent on the 100Fe10Mo than on the 100Fe5Mo catalyst.

Table 1
XPS results of the catalysts.

Catalyst composition	Binding energies (eV)			Nominal Fe/Mo (mol/mol)	Analyzed Fe/Mo (mol/mol)
	$Fe2p_{3/2}$	$Mo3d_{5/2}$	O1*s*		
100Fe	710.4	–	529.7	–	–
100Fe5Mo	710.7	232.0	529.8	100/5	100/13
100Fe10Mo	710.7	232.2	529.9	100/10	100/15
MoO_3	–	232.7	530.5	–	–
100Fe10Mo[a]	709.7	232.0	530.0	100/10	100/18
100Fe10Mo[b]	707.4	228.5	530.0	100/10	100/17

[a] The 100Fe10Mo catalyst was pretreated in syngas (H_2/CO = 0.67) at 280 °C for 12 h.
[b] The 100Fe10Mo catalyst was pretreated in syngas (H_2/CO = 0.67) at 350 °C for 12 h.

3.1.4. Characterization by XPS

XPS characterization was also carried out, as shown in Table 1. For the 100Fe catalyst, the 710.4 eV $Fe2p_{3/2}$ binding energy (BE) was characteristic of the α-Fe_2O_3 phase. With the Mo/Fe nominal ratio increased from 5:100 to 10:100, the $Fe2p_{3/2}$ BE gradually shifted from 710.4 to 710.7 eV, which is within the XPS experimental error. Besides, the analyzed surface Mo/Fe atom ratios in the FeMo catalysts are not much higher than the nominal ones, indicating that the majority of the Mo species remains in the catalyst bulk.

3.2. Surface structure of catalysts after pretreatment

The evolution of phase compositions in the near-surface region of pretreated 100Fe and 100Fe10Mo catalysts was studied by ex situ XPS (Figs. 4 and 5). The BEs of the $Fe2p_{3/2}$ spectrum of pretreated 100Fe (syngas, 350 °C) were at 709.6 and 706.8 eV, which were characteristic of reduced iron oxides (Fe_3O_4, FeO) and iron carbides (FeC_x), respectively (Fig. 4) [20]. In comparison with pretreated 100Fe (syngas, 350 °C), a large peak with a BE at 710.4 eV showed up in the $Fe2p_{3/2}$ spectrum of the 100Fe10Mo catalyst pretreated in syngas at 280 °C, corresponding to the reduced iron oxides (Fe_3O_4, FeO); also, on the low-BE side of this large peak, a small shoulder with BE 706.8 eV appeared, assigned to the iron carbides (FeC_x). With the increase of pretreatment temperature from 280 to 350 °C, the $Fe2p_{3/2}$ peak characteristic of reduced iron oxides turned into a small shoulder, while that of iron carbides developed into an overwhelming peak, which implied that higher pretreatment temperature (350 °C) was more favorable for the carburization of 100Fe10Mo catalyst.

The Mo3*d* spectra of two pretreated 100Fe10Mo catalysts (syngas, 280 °C; syngas, 350 °C) in Fig. 4 were deconvoluted to yield

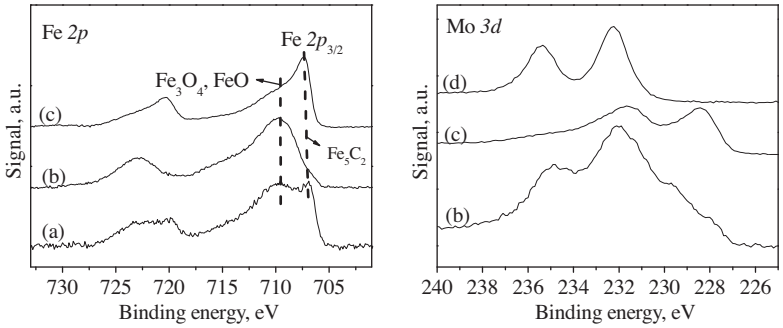

Fig. 4. Fe2*p* and Mo3*d* photoemission spectra: (a) 100Fe pretreated by syngas at 350 °C; (b) 100Fe10Mo pretreated by syngas at 280 °C; (c) 100Fe10Mo pretreated by syngas at 350 °C; (d) 100Fe10Mo after calcination.

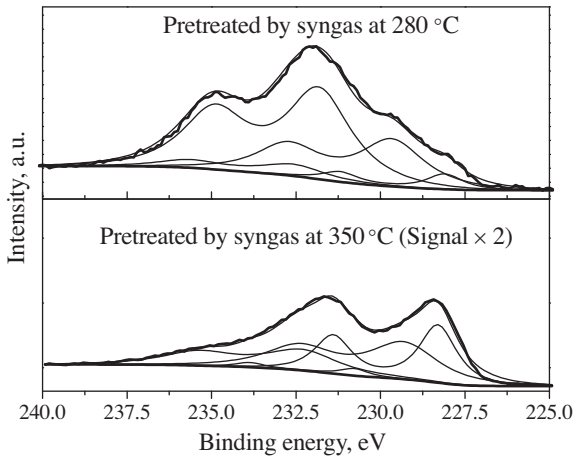

Fig. 5. XPS patterns of Mo3*d* photoemission spectra of pretreated 100Fe10Mo catalysts.

Table 2
Quantitative analysis of Mo3*d* signals for pretreated 100Fe10Mo catalysts.

Catalyst	Pretreatment	Assignment	BE (eV)	Area (%)
100Fe10Mo	280 °C, syngas	Mo^{6+}	232.6	7.2
		Mo^{5+}	231.8	57.3
		Mo^{5+}–Mo^{4+}	229.7	29.7
		Mo^{2+}	228.1	5.8
	350 °C, syngas	Mo^{6+}–Mo^{5+}	232.3	23.0
		Mo^{5+}–Mo^{4+}	230.8	3.3
		Mo^{4+}–Mo^{2+}	229.3	39.0
		Mo^{2+}	228.3	34.7

several Mo ions with different covalents (Mo^{2+}, Mo^{4+}–Mo^{2+}, Mo^{5+}–Mo^{4+}, Mo^{5+}, Mo^{6+}–Mo^{5+} and Mo^{6+}) (see Fig. 5 and Table 2) [53,54]. As shown in Table 2, the majority of Mo oxides in 100Fe10Mo catalyst were reduced to Mo^{4+} and Mo^{5+}–Mo^{4+} after pretreatment in syngas at 280 °C, while most of the Mo species in 100Fe10Mo pretreated in syngas at 350 °C were in the form of Mo^{2+} and Mo^{2+}–Mo^{4+}. Clearly, higher reduction degree of Mo oxides in 100Fe10Mo was achieved at 350 °C than at 280 °C. It is noteworthy that the binding energies of the Mo^{2+} ions in the Mo3$d_{5/2}$ spectra were in the range of 228.1–228.3 eV, which were very close to those reported for the Mo_2C (227.7–228.25 eV) [55]. The positions of Mo3*d* in Mo_2C and Mo^{2+} could not be distinguishable and were considered as single states [56]. Thus, to identify the phase(s) of Mo in pretreated FeMo catalysts, HRTEM measurement was performed, as reported in the next section.

3.3. Structural evolution of catalysts after pretreatment

3.3.1. Evolution of Mo species during pretreatment

Pretreatment-induced evolution in the phase and structure of MoO_x species was characterized by HRTEM, as shown in Figs. 6 and 7. According to their calculated interplanar spacings (4.5 , 4.6 and 4.8 Å) (Figs. 6d, f, and 7b, d, f), the Mo phases in the pretreated FeMo catalysts were identified to be MoO_x species (mixture of Mo_4O_{11} and MoO_2), irrespective of activation protocols.

The structure of MoO_x species was dependent on the pretreatment protocols. After pretreatment in CO, a nanorod-like structure was observed on the surfaces of 100Fe5Mo and 100Fe10Mo catalysts, which can be assigned to the epitaxial crystal growth of MoO_x species from the bulk to the surface of the catalyst (Fig. 7b, d, and f). The epitaxial crystal growth of MoO_x species was more pronounced at the catalyst with a high Mo loading level (100Fe10Mo) or at elevated pretreatment temperature (350 °C): the lengths and widths of the MoO_x nanorods were 8–20 nm and 7–10 nm, respectively, in 100Fe5Mo treated with CO at 280 °C, which increased to 31–95 nm and 17–52 nm, respectively, in 100Fe10Mo activated in CO at 350 °C. No epitaxial crystal growth of MoO_x species was observed in H_2 pretreatment and in syngas pretreatment. Instead, small (average diameter 7 nm) and large (average diameter 13 nm) spherical or elliptical MoO_x particles were observed on H_2- and on syngas-activated FeMo catalysts, respectively (Fig. 6d and f). Overall, the independent identification of the MoO_x species (such as Mo_4O_{11} and MoO_2) closely interacting with iron species has extended our perspective on the Mo promoter nature after various pretreatments to a nanometer resolution; namely there exists a synergistic promotional effect, which is a combination of a physical dispersion effect and an epitaxial crystal growth effect of Mo oxides in the bimetallic FeMo catalysts, which led to the observed complex iron and molybdenum species restructuring during pretreatment and FTS reaction.

3.3.2. Effect of Mo evolution on the size of iron carbides

The HRTEM images of the 100Fe5Mo and 100Fe10Mo catalysts after various pretreatments are displayed in Figs. 6 and 7. The calculated interplanar spacings of the iron particles in the pretreated FeMo catalysts were in the ranges of 2.4–2.5 and 2.7–2.8 Å, which can be attributed to the (3 1 1) plane of Fe_3O_4 and the (3 1 $\bar{1}$) plane of χ-Fe_5C_2, respectively (Fig. 7b and f).

The average size of iron active crystallites (Fe^0 or χ-Fe_5C_2) in the FeMo catalysts was influenced by the pretreatment protocols and Mo loading levels. The average size of iron active crystallites was 12 nm in the 100Fe5Mo catalyst when it was pretreated in CO at 280 °C, which increased to 14 nm and 13 nm when pretreated in H_2 at 350 °C and in syngas at 350 °C, respectively (Figs. 6a, b and 7a). This trend was also observed on the CO- or syngas-pretreated 100Fe10Mo catalysts. The mean average size of iron carbides in the 100Fe10Mo catalyst was 9 nm when pretreated in CO at 280 °C, which increased to 12 nm and 26 nm when pretreated in syngas and in CO at 350 °C, respectively (Figs. 6e and 7c and e). However, no obvious increase in the average size of iron crystallites was observed on the 100Fe10Mo catalysts when they were pretreated in H_2 at 350 °C. The average size of iron crystallites of the 100Fe10Mo pretreated in H_2 at 350 °C was 10 nm, much smaller than those of 100Fe10Mo pretreated in CO or syngas at 350 °C (Fig. 6c).

Pretreatment in CO or in syngas at 350 °C caused obvious epitaxial crystal growth or agglomeration of Mo species from the bulk to the surface of the catalyst, leading to a separation between Fe and Mo phases. This would on the one hand lead to the agglomeration of χ-Fe_5C_2 particles into large particles (12–26 nm) and on the other hand to small iron carbides formed along with MoO_x nanorods during phase separation of Fe and Mo, as can be clearly seen from Fig. 7e, in which small iron particles with an estimated average diameter of 12 nm were observed scattering on round the MoO_x nanorods in the 100Fe10Mo catalyst treated with CO at 350 °C.

In comparison with 350 °C, pretreatment in CO or syngas at 280 °C only caused mild epitaxial crystal growth or agglomeration of MoO_x species, and the majority of MoO_x species were still left in the bulk of the catalysts, leading to the formation of small iron crystallites. In comparison with CO or syngas activation, MoO_x species were highly dispersed after H_2 pretreatment, which would suppress the agglomeration of iron active particles.

3.4. Reduction/carburization of catalysts after pretreatment and FTS reaction

3.4.1. Mössbauer spectroscopy at 298 K

The bulk iron phases in the pretreated catalysts and used catalysts (after nearly 200 h of reaction) were quantitatively characterized by MES (see Table 3 and Figs. S2–S5). FeMo catalyst

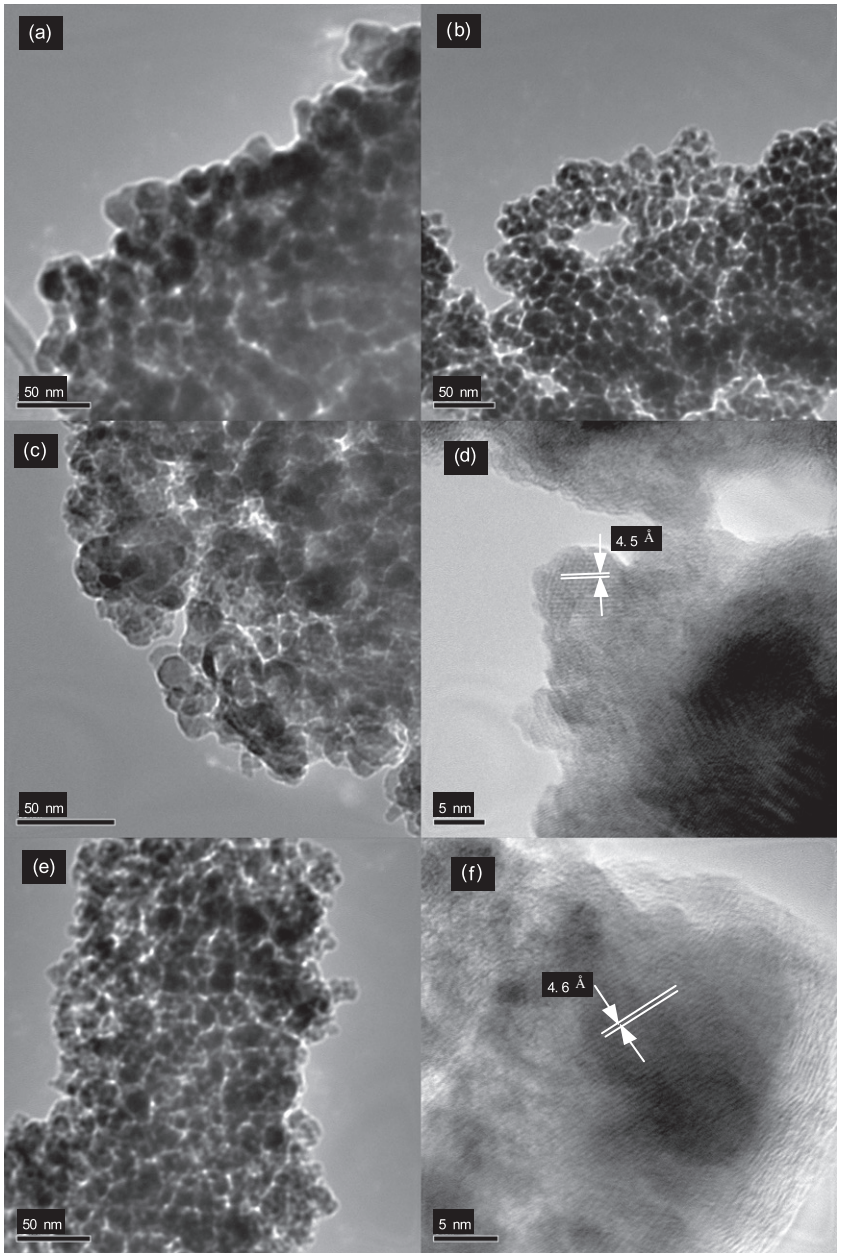

Fig. 6. HRTEM micrographs of FeMo catalysts after H_2 and after syngas pretreatments: (a) 100Fe5Mo pretreated in H_2 at 350 °C; (b) 100Fe5Mo pretreated in $H_2/CO = 0.67$ at 350 °C; (c, d) 100Fe10Mo pretreated in H_2 at 350 °C; (e, f) 100Fe10Mo pretreated in $H_2/CO = 0.67$ at 350 °C.

precursors subjected to H_2 pretreatment were reduced mainly to α-Fe and Fe_3O_4, which were transformed into $\acute{\varepsilon}$-$Fe_{2.2}C$ after further exposure to the reaction environment. In contrast, χ-Fe_5C_2 was the only carbide phase found on the FeMo catalysts pretreated in CO or in syngas after FT reactions for 200 h. After pretreatment in CO or syngas at 350 °C, more iron carbide phases were formed in 100Fe5Mo than in 100Fe10Mo, indicating that Mo promoter inhibited the carburization of iron catalysts [29,33], whereas this rank in the content of iron carbides was reversed for these two catalysts at a lower pretreatment temperature of 280 °C; namely more iron carbides were formed in 100Fe10Mo catalyst than in 100Fe5Mo counterparts (Table 3). As HRTEM characterization showed that smaller iron oxide was observed in 100Fe10Mo catalyst precursor than in with 100Fe5Mo catalyst precursor, this enhanced carburization in 100Fe10Mo catalyst may be due to the presence of smaller iron crystallites, which facilitated carbide formation at a low temperature of 280 °C.

3.4.2. Mössbauer spectroscopy at 20 K

3.4.2.1. SPM iron particles. After pretreatment, MES at 298 K indicated that about 2–10% and 12–20% of iron phases existed in the form of superparamagnetic (SPM) species (Fe^{3+} and/or Fe^{2+}) in 100Fe5Mo and 100Fe10Mo, respectively, while no SPM iron species were observed on the pretreated 100Fe catalyst (Table 3). To accurately identify the phases of these small-sized iron particles, MES was performed at a low temperature of 20 K.

The Mössbauer spectra and the distributions of iron phases in the pretreated catalysts measured by MES at 20 K are displayed in Figs. S6 and S7 and Figs. 8 and 9, respectively. In some cases, to improve the fitting of the central portion of the χ-Fe_5C_2 spectra, a quadrupole-split doublet was added in the final computer fit, which was assigned to a superparamagnetic χ-Fe_5C_2 [57]. When pretreated at 280 °C, the SPM iron species in the FeMo catalysts were verified to be Fe_3O_4 nanoparticles irrespective of pretreatment gas type, as indicated by an increase in the content of

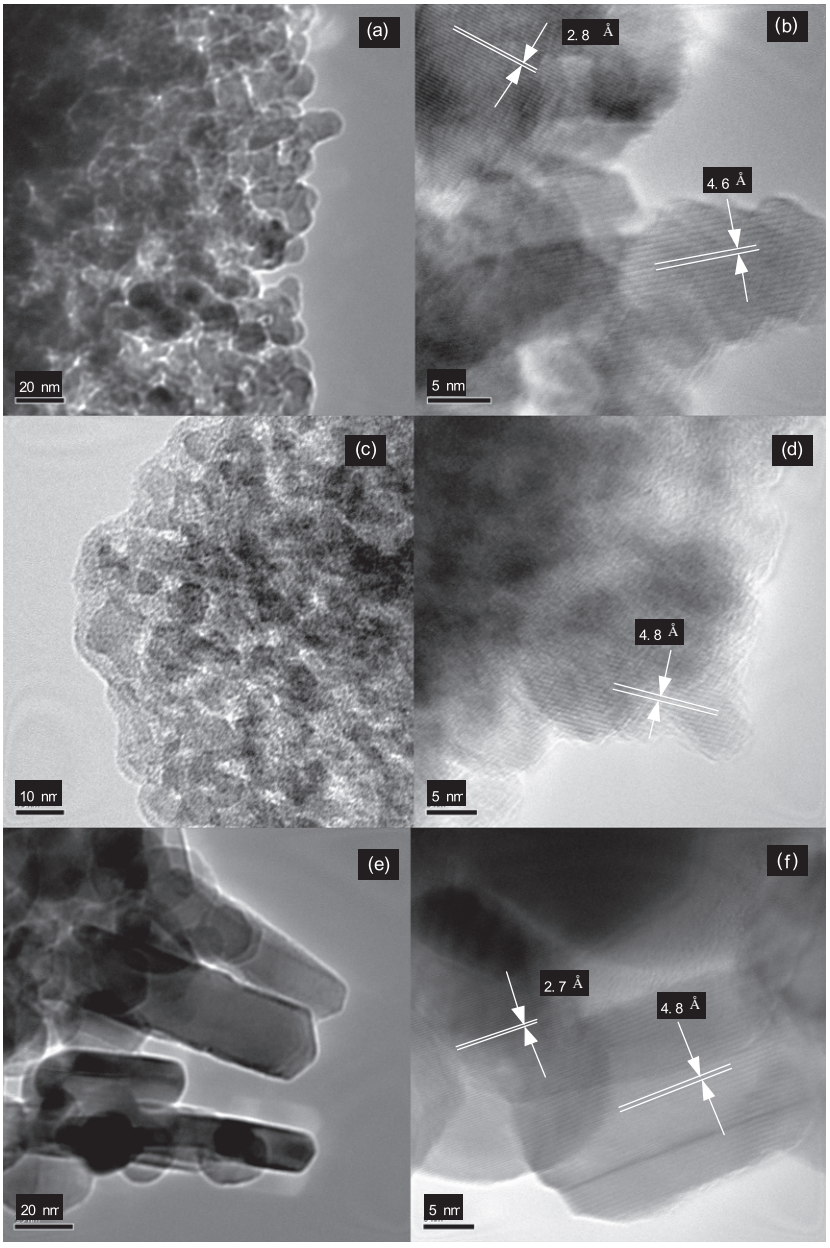

Fig. 7. HRTEM micrographs of FeMo catalysts after CO pretreatment: (a, b) 100Fe5Mo pretreated in CO at 280 °C; (c, d) 100Fe10Mo pretreated in CO at 280 °C; (e, f) 100Fe10Mo pretreated in CO at 350 °C.

magnetite in the catalyst (Fig. 8). An exception was observed in the 100Fe10Mo catalyst pretreated in H_2 at 280 °C, in which the SPM iron species were identified to be ultrafine α-Fe particles. When pretreated at 350 °C, the phase of the SPM iron particles in the FeMo catalysts was dependent on the pretreatment gas types: SPM Fe_3O_4 for H_2 pretreatment and SPM χ-Fe_5C_2 for CO or syngas pretreatment (Fig. 9). Near the blocking temperature at which half of the particles exhibit SPM relaxation, KV/k_BT has an average value of 4.5 [46]. Taking the anisotropy energy constant K values of $(0.9 \pm 0.3) \times 10^5$ J/m^3 [43] and $(1.2 \pm 0.2) \times 10^5$ J/m^3 [58], the approximate average sizes of SPM Fe_3O_4 and SPM α-Fe crystallites were evaluated to be 5 nm and 3 nm, respectively, while taking an anisotropy energy constant K value of 1.3×10^5 J/m^3 [59] for the SPM χ-Fe_5C_2 crystallites in 100Fe10Mo catalyst pretreated in CO at 350 °C resulted in a mean diameter of 5 nm. The result of SPM χ-Fe_5C_2 crystallites was in good agreement with the observation of small iron crystallites in the pretreated FeMo catalysts by HRTEM; namely, small iron crystallites were observed scattering round the MoO_x species. The mean diameter of these small iron crystallites estimated by HRTEM (12 nm) was larger than that estimated by MES, which may be due to the overlapping between these SPM iron carbides to form large "clusters."

3.4.2.2. Stability of bulk and SPM iron carbides during FTS reaction. The distributions of iron phases in the post mortem catalysts and their Mössbauer parameters measured by MES at 20 K are displayed in Fig. 10. For 100Fe and FeMo catalysts, the content of the χ-Fe_5C_2 phase was 100.0% after pretreatment in syngas or CO at 350 °C. This content, however, decreased sharply to only 13.5% for post mortem 100Fe catalyst, while this content was 72.2% for 100Fe5Mo and 100.0% for 100Fe10Mo catalyst after the FTS reaction (time on stream (TOS) = 192 h) (Fig. 10 and Table 3). This indicated that the Mo promoter improved the stability of bulk iron carbides in the FeMo catalyst, and the stabilization effect of Mo

Table 3
Mössbauer parameters of 100Fe5Mo and 100Fe10Mo after pretreatment and after FTS reaction.

Run No.	Phases	After pretreatment		Phases	After FTS reaction	
		100Fe5Mo Area (%)	100Fe10Mo Area (%)		100Fe5Mo Area (%)	100Fe10Mo Area (%)
H_2, 280 °C	α-Fe	22.1	10.2	ε′-$Fe_{2.2}C$	26.7	40.7
	Fe_3O_4	77.9	79.4	Fe_3O_4	71.4	48.1
	Fe (spm)[a]	–	10.4	Fe (spm)[a]	1.9	11.2
H_2, 350 °C	α-Fe	81.0	51.9	ε′-$Fe_{2.2}C$	41.0	70.8
	Fe_3O_4	14.9	42.2	Fe_3O_4	55.1	22.0
	Fe (spm)[a]	4.1	5.9	Fe (spm)[a]	3.9	7.2
CO, 280 °C	χ-Fe_5C_2	66.3	72.5	χ-Fe_5C_2	36.4	70.7
	Fe_3O_4	25.5	–	Fe3O4	60.6	11.0
	Fe (spm)[a]	8.2	27.5	Fe (spm)[a]	3.0	18.3
CO, 350 °C	χ-Fe_5C_2	97.3	79.1	χ-Fe_5C_2	81.2	79.6
	Fe (spm)[a]	2.7	–	Fe_3O_4	14.3	–
	Fe (spm)[a]	–	20.9	Fe (spm)[a]	4.5	20.4
Syngas, 280 °C	χ-Fe_5C_2	28.5	64.9	χ-Fe_5C_2	29.1	72.7
	Fe_3O_4	64.0	10.1	Fe_3O_4	69.2	10.7
	Fe (spm)[a]	7.5	25.0	Fe (spm)[a]	1.7	16.6
Syngas, 350 °C	χ-Fe_5C_2	93.3	82.7	χ-Fe_5C_2	82.0	78.5
	Fe_3O_4	–	–	Fe_3O_4	11.7	–
	Fe (spm)[a]	6.7	17.3	Fe (spm)[a]	6.3	21.5

[a] Fe (spm) includes Fe^{3+} (spm) and Fe^{2+} (spm).

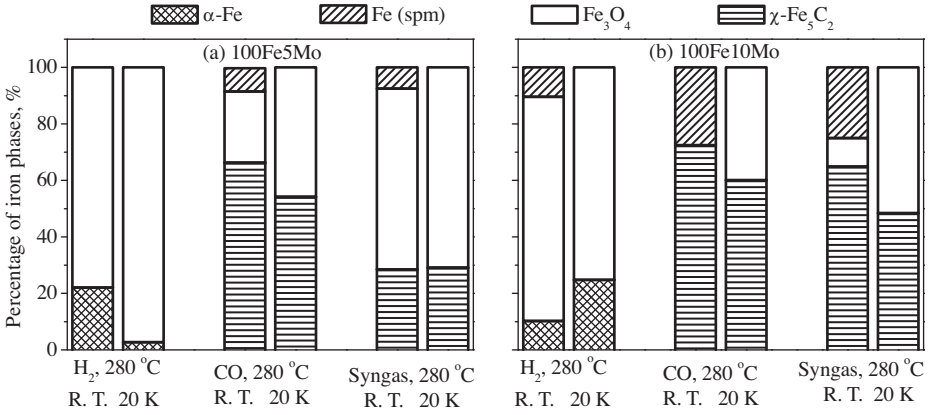

Fig. 8. Comparison of percentages of iron phases measured by MES at 298 K and 20 K in the FeMo catalysts pretreated at 280 °C: (a) 100Fe5Mo; (b) 100Fe10Mo.

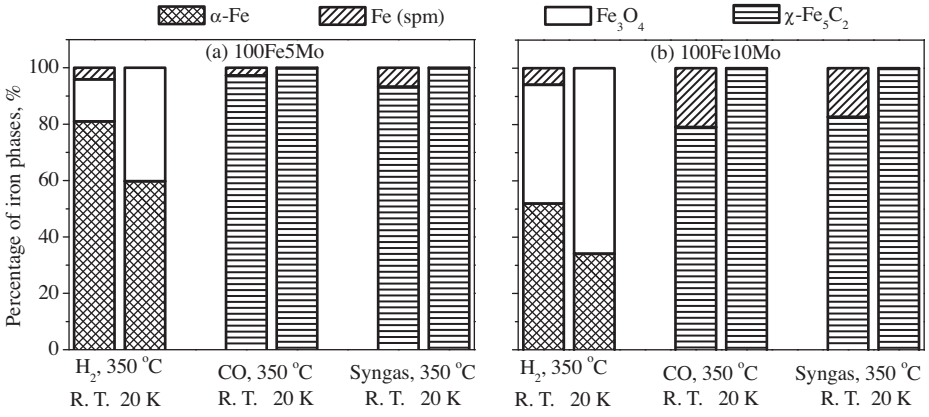

Fig. 9. Comparison of percentages of iron phases measured by MES at 298 K and 20 K in the FeMo catalysts pretreated at 350 °C: (a) 100Fe5Mo; (b) 100Fe10Mo.

was enhanced as the Mo loading level increased. Furthermore, the stabilization of SPM χ-Fe_5C_2 crystallites was enhanced with additional Mo. For instance, the SPM χ-Fe_5C_2 crystallites in the pretreated 100Fe5Mo catalysts (CO, 350 °C; syngas, 350 °C) were reoxidized to SPM Fe_3O_4 crystallites, whereas the SPM χ-Fe_5C_2 crystallites in the activated 100Fe10Mo catalysts (CO, 350 °C; syngas, 350 °C) showed high stability even after roughly 200 h of FTS reaction (Fig. 10). As indicated by HRTEM, larger MoO_x particles

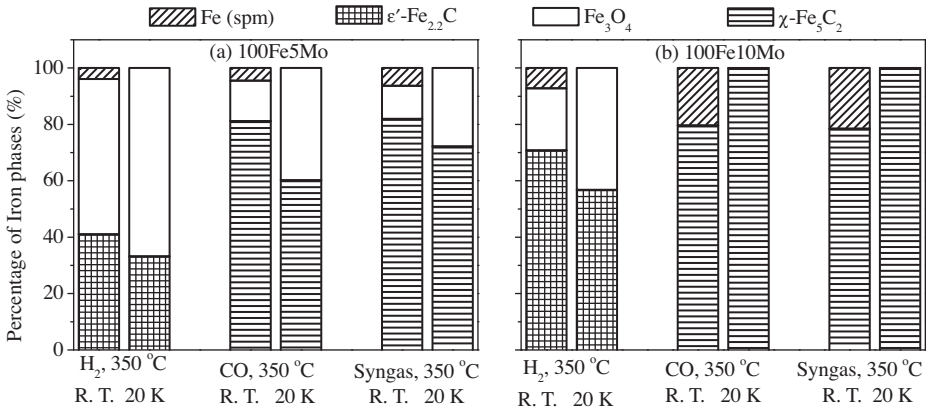

Fig. 10. Comparison of percentages of iron phases measured by MES at 298 K and 20 K in the post mortem FeMo catalysts pretreated at 350 °C: (a) 100Fe5Mo; (b) 100Fe10Mo.

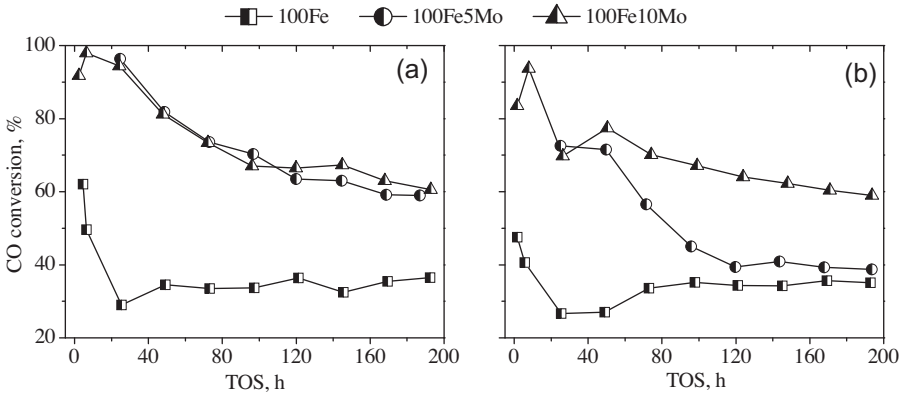

Fig. 11. CO conversions of all catalysts pretreated in H_2 at (a) 280 °C; (b) 350 °C.

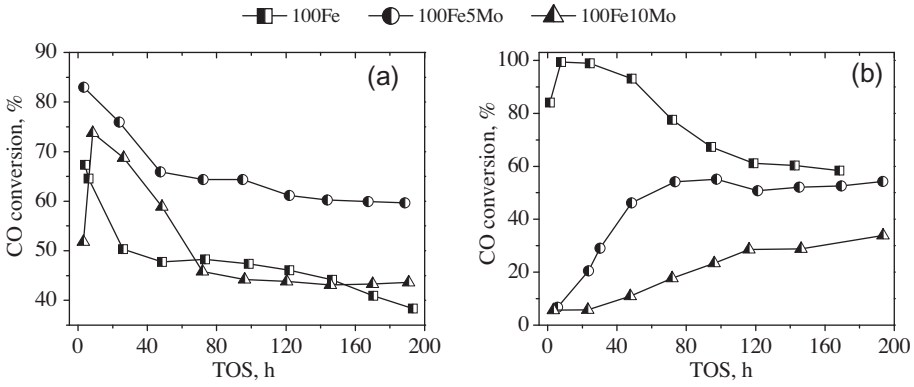

Fig. 12. CO conversions of Fe and FeMo catalysts pretreated in $H_2/CO = 0.67$ at (a) 280 °C; (b) 350 °C.

or nanorods formed on the 100Fe10Mo catalysts activated in CO or syngas at 350 °C than on the 100Fe5Mo counterparts. Hence, it appeared that the SPM χ-Fe_5C_2 crystallites scattering on round large-sized MoO_x species showed higher stability.

3.5. FTS performances: activity and selectivity

The MoO_x species exhibit no FT activity [29]. However, pretreatment-induced evolution in the promotional effects of the MoO_x species, as implied by HRTEM and MES characterization, influenced the nature of active iron particles, which may consequently influence the catalytic performances. This expectation was confirmed by the catalytic measurements reported in this section.

The FTS performances of all the catalysts is presented in Figs. 11–13 and Table 4. The CO conversion was used as a measurement of FTS reactivity for all fixed-bed FTS runs.

For 100Fe catalyst, the activity decreased with time on stream, irrespective of pretreatment protocols. Besides, the stable activities after treatment with H_2 were lower than those of syngas-pretreated counterparts, probably because the sintering of α-Fe particles occurred during H_2 pretreatment (Figs. 11 and 12) [10]. In contrast, H_2-pretreated FeMo catalysts showed higher stable activity than

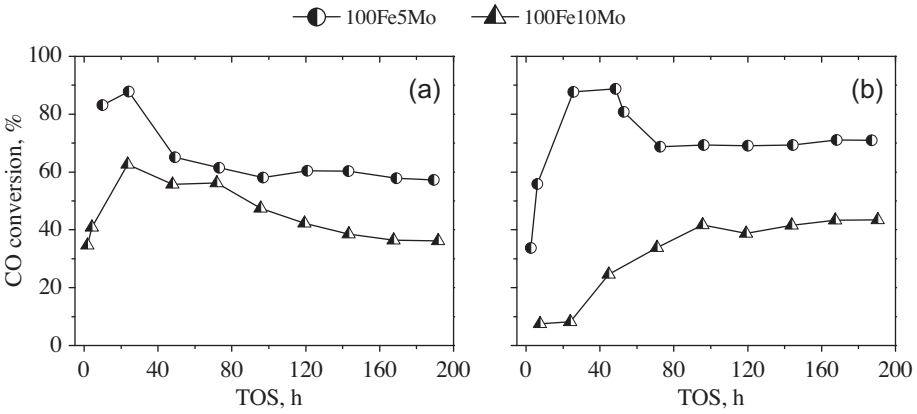

Fig. 13. CO conversions of FeMo catalysts pretreated in CO at (a) 280 °C; (b) 350 °C.

Table 4
Effect of pretreatment procedures on the FTS performances of the catalysts.[a]

Catalyst	100Fe		100Fe5Mo					100Fe8Mo	100Fe10Mo						
Activation temperature (°C)	350	350	280	280	350	350	350	350	280	280	280	350	350	325	350
Activation gas	H_2	Syngas	H_2	CO	H_2	CO	Syngas	Syngas	H_2	CO	Syngas	H_2	CO	Syngas	Syngas
TOS, h	193	168	187	189	194	187	193	192	193	192	191	194	190	192	194
CO conversion (%)	35.1	58.4	59.0	57.3	49.7	71.0	54.2	34.0	60.5	36.2	43.6	59.0	43.4	33.8	33.9
H_2/CO in tail gas	1.5	2.0	2.2	2.1	2.3	2.6	2.1	1.7	2.3	1.7	1.8	2.2	1.7	1.7	1.6
$K_p(P_{CO_2} \cdot P_{H_2})/(P_{CO} \cdot P_{H_2O})$	0.6	1.2	4.6	3.8	2.1	4.3	2.2	1.7	5.1	1.8	2.1	5.3	1.3	2.1	1.1
CO_2 selectivity	25.5	27.8	46.4	45.4	32.6	42.4	30.8	42.1	42.7	34.9	32.2	46.7	34.1	40.2	28.1
Selectivities (wt.%)															
CH_4	18.0	16.8	28.6	29.3	26.7	23.4	24.4	21.8	31.0	32.5	29.9	28.2	15.9	23.6	14.0
C_{2-4}	42.6	37.3	52.2	44.1	53.4	39.5	41.2	39.0	51.7	45.5	42.4	51.8	31.0	38.6	26.8
C_{5-11}	29.2	32.9	16.4	24.0	18.1	28.4	24.3	28.0	13.9	17.7	19.7	14.5	33.7	37.8 [c]	28.8
C_{12-18}	5.9	7.5	0.9	1.4	1.5	4.5	7.0	7.9	2.1	3.2	4.5	3.0	12.5	–	14.7
C_{19+}	4.3	5.5	1.9	1.2	0.3	4.2	3.1	3.3	1.3	1.1	3.5	2.5	6.9	–	15.7
$C_2^=-C_4^=/C_2^o - C_4^o$ (mol/mol)	0.8	1.0	0.5	0.4	0.5	0.7	0.7	0.9	0.4	0.5	0.6	0.4	1.1	0.9	1.2
Alcohols (wt.%) [b]	8.1	8.6	4.6	6.1	12.1	7.0	3.9	8.4	7.8	11.9	10.0	6.6	12.2	–	15.1

[a] Reaction condition: 280 °C, 1.5 MPa, H_2/CO = 1.6 and GHSV = 3000 h^{-1}.
[b] Alcohols in total hydrocarbon and oxygenates.
[c] C_5^+ selectivity.

H_2-pretreated 100Fe catalyst (Fig. 11). This improvement in the stable activity was more pronounced on 100Fe10Mo catalyst. The higher activity of H_2-pretreated FeMo catalysts was due to the dispersive effect of Mo on the active iron sites, which suppressed the sintering of active iron sites. Another obvious trend observed in Figs. 11–13 was that the CO or syngas pretreatment of 100Fe10Mo catalyst resulted in much lower stable activity than that of the H_2-pretreated catalysts. As indicated by HRTEM, reduced MoO_x species agglomerated to form large particles in syngas pretreatment, or to form large nanorods in CO pretreatment on the FeMo catalyst surface at an elevated activation temperature (350 °C) or at a high Mo loading level, which led to several consequences: (1) the dispersion effect of MoO_x species was weakened to a large extent, which in turn caused an agglomeration of active iron crystallites; (2) MoO_x species (either large particles or nanorods) were enriched on the surface of the catalyst, which as a result covered part of the iron active sites. Overall, the epitaxial crystal growth of MoO_x species caused a decrease in the available active iron sites and consequently a loss of catalytic activity. This explained the low stable activity observed on the 100Fe10Mo catalysts after activation in CO or in syngas. For 100Fe5Mo, the epitaxial crystal growth of MoO_x species would be much less obvious due to its low Mo loading level. Thus, higher stable activity was found on the 100Fe5Mo catalysts after pretreatment in CO or in syngas than on the 100Fe10Mo counterparts.

Furthermore, the product distributions of 100Fe5Mo catalysts shifted toward methane and light hydrocarbons (C_2–C_4) in comparison with 100Fe catalyst, while the product distributions of 100Fe10Mo catalyst were dependent on both the Mo promoter and pretreatment procedures. As can be seen from Table 4, 100Fe10Mo pretreated at 280 °C (H_2, CO, or syngas) or pretreated in H_2 at 350 °C showed product distributions similar to those of 100Fe5Mo, i.e., high selectivity toward methane and C_2–C_4 hydrocarbons, whereas unexpected product distributions were observed on 100Fe10Mo catalysts after pretreatment in CO or syngas at 350 °C, i.e., the selectivities to methane, light gases (C_2–C_4) and gasoline fractions (C_5–C_{11}) were lower than those of 100Fe activated in syngas at 350 °C, while the selectivities to diesel and wax fractions (C_{12}^+) were twice as high as those of 100Fe activated in syngas at 350 °C (Table 4). This improved selectivity to heavy hydrocarbons observed on 100Fe10Mo catalysts pretreated in CO or syngas at 350 °C did not result from low catalyst activities. For example, the FT selectivity of 100Fe10Mo pretreated in CO or syngas at 280 °C was quite different from that pretreated in CO or syngas at 350 °C even though they showed similar activities (Table 4). It appeared that the catalyst selectivity was determined by the nature of active iron carbides, which was shaped by the pretreatment-induced migration of Mo. As discussed above, the MoO_x species were still dispersed in the FeMo catalysts after pretreatment in H_2, while activation in syngas or

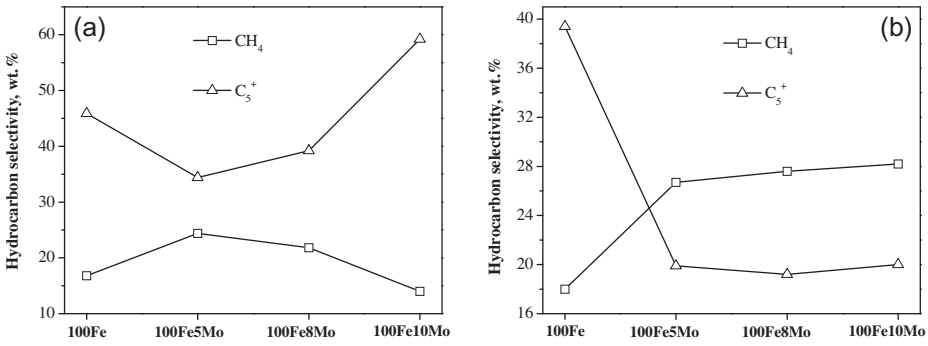

Fig. 14. Hydrocarbon selectivity of Fe and FeMo catalysts pretreated at 350 °C in (a) $H_2/CO = 0.67$; (b) H_2.

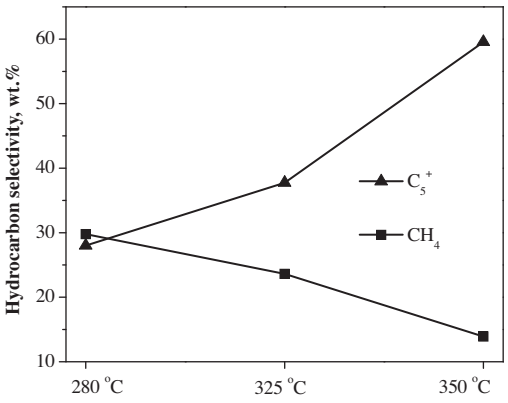

Fig. 15. Hydrocarbon selectivity of 100Fe10Mo catalyst pretreated in $H_2/CO = 0.67$ at various temperatures.

CO at 280 °C caused a mild agglomeration or epitaxial crystal growth of the MoO_x species, and the majority of MoO_x species remained in the bulk of the catalyst. Hence, the active iron sties after these pretreatments closely interact with MoO_x species, and the nature of active iron sites was modified by neighboring Mo species, leading to a shift in FT selectivity to light hydrocarbons. On the contrary, pretreated in CO or syngas at 350 °C led to a severe agglomeration or epitaxial crystal growth of MoO_x species in the FeMo catalysts, which resulted in partial separation between active iron carbides and MoO_x species and consequently more "pure" iron carbide performances. Furthermore, these active iron carbide crystallites (bulk and SPM) were well stabilized by Mo species during the FTS reaction; i.e., their size distributions and local environments (with fewer neighboring Mo species) were stable under the FTS conditions. Hence, the FT selectivity shifted toward heavy hydrocarbons. To verify this assumption, two sets of fixed-bed FTS runs were carried out. One was on the effect of different Mo loading levels for a family of FeMo catalysts; the other was to check the effect of pretreatment temperature on the syngas-pretreated 100Fe10Mo catalyst. These experiments were based on the HRTEM observation that the epitaxial crystal growth of MoO_x species in the FeMo catalysts was more pronounced in either at a high Mo loading level or at elevated pretreatment temperatures. Test results are shown in Figs. 14 and 15 and Table 4. The selectivity to CH_4 of the FeMo catalyst pretreated in syngas at 350 °C gradually decreased, while that to C_5^+ increased with increased catalyst Mo loading levels (Fig. 14a). However, this trend was not observed for catalysts pretreated in H_2 at 350 °C, where both CH_4 and C_5^+ selectivities followed the opposite directions (Fig. 14b). The latter result could be explained by the better dispersed Mo species in the catalyst after pretreatment in H_2, and hence the more pronounced interaction between active iron carbides and Mo species with the increasing Mo loading level. Furthermore, increasing pretreatment temperature, an increase in C_5^+ selectivity and a decrease in CH_4 were found on 100Fe10Mo catalyst when pretreated in syngas, as displayed in Fig. 15.

4. Conclusions

During pretreatment, the catalyst structure experienced an extensive restructuring process that was strongly dependent on a synergistic effect of the pretreatment and Mo promoter loading level. An epitaxial crystal growth or agglomeration of Mo species in CO or syngas at 350 °C caused phase separation between Fe and Mo, which on the one hand led to the agglomeration of iron carbide particles (12–26 nm) with fewer neighboring Mo species and on the other hand to the formation of SPM iron carbide particles (5–6 nm) along with large Mo species. In contrast, such Mo species migration was mild after pretreatment in CO or syngas at 280 °C. The majority of Mo remained in the bulk catalyst, leading to the formation of small-sized iron carbide particles. During pretreatment in H_2, the well-dispersed Mo species in the catalyst facilitated the formation of surface active iron surface particles of small size, which interacted closely with the nearby Mo species. Generally, the dispersion effect of Mo promoter inhibited the agglomeration of active iron sites, which resulted in high catalyst activity. In contrast, the epitaxial crystal growth effect that happened at an elevated pretreatment temperature, or a high Mo loading level caused a decrease in the available surface iron sites and consequently a loss in catalytic activity. The epitaxial crystal growth effect of Mo promoter during pretreatment exhibited a twofold effect: on the one hand, it negatively influenced the catalyst activity, and on the other hand, it improved the catalyst selectivity in the current study, i.e., causing lower selectivity to C_1–C_4 and higher selectivity to C_{12}^+.

Acknowledgments

We thank the National Outstanding Young Scientists Foundation of China (20625620) and the National Natural Science Foundation of China (20703054 and 20590361). This work is also supported by Synfuels China Co., Ltd.

Appendix A. Supplementary material

Supplementary data associated with this article can be found, in the online version, at doi:10.1016/j.jcat.2011.05.020.

References

[1] Y.W. Li, J. Xu, Y. Yang, in: A.A. Vertès, N. Qureshi, H.P. Blaschek, H. Yukama (Eds.), Biomass to Biofuels: Strategies for Global Industries, John Wiley & Sons, 2010, p. 123 (Chapter 6).
[2] E. de Smit, B.M. Weckhuysen, Chem. Soc. Rev. 37 (2008) 2758.
[3] Y. Yang, H.W. Xiang, L. Tian, H. Wang, C.H. Zhang, Z.C. Tao, Y.Y. Xu, B. Zhong, Y.W. Li, Appl. Catal. A Gen. 284 (2005) 105.
[4] C.H. Zhang, Y. Yang, B.T. Teng, T.Z. Li, H.Y. Zheng, H.W. Xiang, Y.W. Li, J. Catal. 237 (2006) 405.
[5] N. Lohitharn, J.G. Goodwin Jr., J. Catal. 257 (2008) 142.
[6] N. Lohitharn, J.G. Goodwin Jr., J. Catal. 260 (2008) 7.
[7] D.B. Bukur, L. Nowicki, X.S. Lang, Energy Fuels 9 (1995) 620.
[8] D.B. Bukur, X.S. Lang, J.A. Rossin, W.H. Zimmerman, M.P. Rosynek, E.B. Yeh, C.P. Li, Ind. Eng. Chem. Res. 28 (1989) 1130.
[9] D.B. Bukur, M. Koranne, X.S. Lang, K.R.P.M. Rao, G.P. Huffman, Appl. Catal. A Gen. 126 (1995) 85.
[10] D.B. Bukur, X.S. Lang, Y.J. Ding, Appl. Catal. A Gen. 186 (1999) 255.
[11] M.D. Shroff, D.S. Kalakkad, K.E. Coulter, S.D. Köhler, M.S. Harrington, N.B. Jackson, A.G. Sault, A.K. Datye, J. Catal. 156 (1995) 185.
[12] M.S. Luo, B.H. Davis, Fuel Process. Technol. 83 (2003) 49.
[13] M.S. Luo, H. Hamdeh, B.H. Davis, Catal. Today 140 (2009) 127.
[14] M.Y. Ding, Y. Yang, J. Xu, Z.C. Tao, H.L. Wang, H. Wang, H.W. Xiang, Y.W. Li, Appl. Catal. A Gen. 345 (2008) 176.
[15] M.Y. Ding, Y. Yang, B.S. Wu, J. Xu, C.H. Zhang, H.W. Xiang, Y.W. Li, J. Mol. Catal. A Chem. 303 (2009) 65.
[16] Q.L. Hao, F.X. Liu, H. Wang, J. Chang, C.H. Zhang, L. Bai, H.W. Xiang, Y.W. Li, F. Yi, B.F. Xu, J. Mol. Catal. A Chem. 261 (2007) 104.
[17] R.J. O'Brien, L.G. Xu, R.L. Spicer, B.H. Davis, Energy Fuels 10 (1996) 921.
[18] J. Xu, C.H. Bartholomew, J. Sudweeks, D.L. Eggett, Top. Catal. 26 (2003) 55.
[19] D.B. Bukur, L. Nowicki, R.K. Manne, X.S. Lang, J. Catal. 155 (1995) 366.
[20] J.B. Butt, Catal. Lett. 7 (1990) 61.
[21] J. Xu, C.H. Bartholomew, J. Phys. Chem. B 109 (2005) 2392.
[22] G.Z. Bian, A. Oonuki, Y. Kobayashi, N. Koizumi, M. Yamada, Appl. Catal. A Gen. 219 (2001) 13.
[23] G.Z. Bian, A. Oonuki, N. Koizumi, H. Nomoto, M. Yamada, J. Mol. Catal. A Chem. 186 (2002) 203.
[24] S.Z. Li, W.P. Ding, G.D. Meitzner, E. Iglesia, J. Phys. Chem. B 106 (2002) 85.
[25] J.F. Schulz, F.S. Karn, R.B. Anderson, US Bureau of Mines, 1967.
[26] K.Y. Park, W.K. Seo, J.S. Lee, Catal. Lett. 11 (1991) 349.
[27] J.W. Dun, E. Gulari, K.Y.S. Ng, Appl. Catal. 15 (1985) 247.
[28] S.T. Liu, A.C. Gujar, P. Thomas, H. Toghiani, M.G. White, Appl. Catal. A Gen. 357 (2009) 18.
[29] W.P. Ma, E.L. Kugler, J. Wright, D.B. Dadyburjor, Energy Fuels 20 (2006) 2299.
[30] W.P. Ma, E.L. Kugler, D.B. Dadyburjor, Stud. Surf. Sci. Catal. 163 (2007) 125.
[31] N. Lohitharn, J.G. Goodwin Jr., E. Lotero, J. Catal. 255 (2008) 104.
[32] A. Septúlveda-Escribano, F. Rodríguez-Reinoso, J. Mol. Catal. 90 (1994) 291.
[33] S.D. Qin, C.H. Zhang, J. Xu, B.S. Wu, H.W. Xiang, Y.W. Li, J. Mol. Catal. A Chem. 304 (2009) 128.
[34] J.W. Niemantsverdriet, A.M. van der Kraan, W.N. Delgass, M.A. Vannice, J. Phys. Chem. 89 (1985) 67.
[35] F. Bødker, S. Mørup, J.W. Niemantsverdriet, Catal. Lett. 13 (1992) 195.
[36] J.A. Amelse, L.H. Schwartz, J.B. Butt, J. Catal. 72 (1981) 95.
[37] G.B. Raupp, W.N. Delgass, J. Catal. 58 (1979) 337.
[38] J.W. Niemantsverdriet, J. van Grondelle, A.M. van der Kraan, Hyperfine Interact. 28 (1986) 867.
[39] W. Kündig, H. Bömmel, Phys. Rev. 142 (1966) 327.
[40] S. Mørup, J. Magn. Magn. Mater. 37 (1983) 39.
[41] S. Mørup, F. Bødker, J. van Wonterghem, M.B. Madsen, M.D. Bentzon, Hyperfine Interact. 51 (1989) 1071.
[42] S. Mørup, Hyperfine Interact. 60 (1990) 959.
[43] S. Mørup, H. Topsøe, Appl. Phys. 11 (1976) 63.
[44] F. Bødker, M.F. Hansen, C.B. Koch, K. Lefmann, S. Mørup, Phys. Rev. B 61 (2000) 6826.
[45] F. Bødker, S. Mørup, Europhys. Lett. 52 (2000) 217.
[46] A.F. Lehlooh, S.H. Mahmood, J. Magn. Magn. Mater. 151 (1995) 163.
[47] Y. Yang, H.W. Xiang, Y.Y. Xu, L. Bai, Y.W. Li, Appl. Catal. A Gen. 266 (2004) 181.
[48] Y.Y. Ji, H.W. Xiang, J.L. Yang, Y.Y. Xu, Y.W. Li, B. Zhong, Appl. Catal. A Gen. 214 (2001) 77.
[49] M.D. Lee, J.F. Lee, C.S. Chang, Appl. Catal. 72 (1991) 267.
[50] D.L.A. de Faria, S.V. ncio Silva, M.T. de Oliveira, J. Raman Spectrosc. 28 (1997) 873.
[51] Charles G. Hill Jr., J.H. Wilson III, J. Mol. Catal. 63 (1990) 65.
[52] D.S. Kim, K. Segawa, T. Soeya, I.E. Wachs, J. Catal. 136 (1992) 539.
[53] M. Yamada, J. Yasumaru, M. HouaUa, D.M. Hercules, J. Phys. Chem. 95 (1991) 7037.
[54] R.B. Quincy, M. Houalla, A. Proctor, D.M. Hercules, J. Phys. Chem. 94 (1990) 1520.
[55] P. Delporte, C. Pham-Huu, M.J. Ledoux, Appl. Catal. A Gen. 149 (1997) 151.
[56] F. Solymosi, A. Oszkó, T. Bánsági, P. Tolmacsov, J. Phys. Chem. B 106 (2002) 9613.
[57] G.B. Raupp, W.N. Delgass, J. Catal. 58 (1979) 348.
[58] F. Bødker, S. Mørup, M.S. Pedersen, P. Svedlindh, G.T. Jonsson, J.L. Garcia-Palacios, F.J. Lazaro, J. Magn. Magn. Mater. 177–181 (1998) 925.
[59] S.C. Lin, J. Phillips, J. Appl. Phys. 58 (1985) 1943.